Research Article | Vol. 31, No. 26 / 18 Dec 2023 / Optics Express 44424
Optics EXPRESS

# Precise parameter control of multicycle terahertz generation in PPLN using flexible pulse trains

N. H. MATLIS,[1,†] Z. ZHANG,[1,2,†] U. DEMIRBAS,[1,3] C. RENTSCHLER,[1,4,5] K. RAVI,[1] M. YOUSSEF,[1] G. CIRMI,[1,6] M. PERGAMENT,[1] M. EDELMANN,[1] S. M. MOHAMADI,[1] S. REUTER,[1] AND F. X. KÄRTNER[1,4,6,*]

[1]*Center for Free-Electron Laser Science CFEL, Deutsches Elektronen-Synchrotron DESY, Notkestr. 85, 22607 Hamburg, Germany*
[2]*Tsung-Dao Lee Institute, Shanghai Jiao Tong University, Shanghai 200240, China*
[3]*Antalya Bilim University, 07190 Dosemealti, Antalya, Turkey*
[4]*Department of Physics, University of Hamburg, Luruper Chaussee 149, 22761 Hamburg, Germany*
[5]*Max Planck School of Photonics, Hans-Knöll-Straße 1, 07745 Jena, Germany*
[6]*The Hamburg Centre for Ultrafast Imaging, University of Hamburg, Luruper Chaussee 149, 22761 Hamburg, Germany*
[†]Equal contributors
[*]*franz.kartner@desy.de*

**Abstract:** The low (sub %) efficiencies so-far demonstrated for nonlinear optical down-conversion to terahertz (THz) frequencies are a primary limiting factor in the generation of high-energy, high-field THz-radiation pulses (in particular narrowband, multicycle pulses) needed for many scientific fields. However, simulations predict that far higher conversion efficiencies are possible by use of suitably-optimized optical sources. Here we implement a customized optical laser system producing highly-tunable trains of infrared pulses and systematically explore the experimental optimization of the down-conversion process. Our setup, which allows tuning of the energy, duration, number and periodicity of the pulses in the train, provides a unique capability to test predictions of analytic theory and simulation on the parameter dependences for the optical-to-THz difference-frequency generation process as well as to map out, with unprecedented precision, key properties of the nonlinear crystal medium. We discuss the agreements and deviations between simulation and experimental results which, on the one hand, shed light on limitations of the existing theory, and on the other hand, provide the first steps in a recipe for development of practical, high-field, efficiency-optimized THz sources.



## 1. Introduction

Narrowband terahertz radiation with high fields and high spectral intensity are becoming increasingly important for a diverse range of commercial and scientific applications, from the communications industry to material science [1] and particle acceleration [2]. Nonlinear optical down-conversion of lasers to the terahertz regime is a favored approach for generating high-field THz pulses due to the high peak power that is achievable as well as because of the versatility of the laser-based approach for generating the desired spectral and temporal properties. By far, the majority of work in THz generation by nonlinear down conversion has targeted single-cycle THz pulses, which are attractive due to the exceptionally-high electric-field strengths in the multiple MV/cm range that can be achieved [3–7]. Laser-driven multicycle THz sources, by contrast, tend to have lower field strengths, as the energy is more spread out in time, but are more favorable for

#503480 https://doi.org/10.1364/OE.503480
Journal © 2023 Received 25 Aug 2023; revised 13 Nov 2023; accepted 23 Nov 2023; published 14 Dec 2023

Optics EXPRESS

driving resonant processes. These sources, which tend to have more specialized applications, have seen far less development, and until recently, have lagged behind their single-cycle cousins in performance.

The preferred approach for multicycle THz generation is based on quasi-phase matching in periodically-poled lithium niobate (PPLN) which is intrinsically narrowband and benefits from the ultrahigh nonlinear coefficient of the lithium niobate ($LiNbO_3$) material. Over the past decade, dedicated efforts at improving the performance of multicycle THz sources have resulted in several orders of magnitude increases in both conversion efficiency and THz pulse energy [7–17]. Nevertheless, conversion efficiencies have remained in sub-percent range. These results stand in apparent contradiction to simulations which suggest that efficiencies in the multiple-percent regime can be achieved by driving PPLN crystals with laser sources of suitably-tailored spectral and temporal properties [18–21]. The reasons for this contradiction, however, have not been fully investigated, leaving the fundamental limits of the conversion efficiency unclear.

The physics of efficient THz generation by nonlinear down conversion is complicated by several factors. The first of these is the necessity of driving the process far into the cascading regime. Due the orders-of-magnitude difference in photon energy between the optical and THz photons, even a complete, 100% conversion of photons corresponds to an energy conversion of only 0.1% for the sub-THz frequencies that are attractive for controlling magnetic order in materials or driving mm-wave particle accelerators. To reach higher conversion efficiencies therefore requires a process known as "cascading" in which each optical photon produces a large number of THz photons. The transfer of energy back and forth between optical and THz photons that this process represents is naturally complex to describe analytically. For example, the applicability of the "undepleted-pump" approximation, which is a highly useful for simplifying the analytical treatment, is rather questionable for efficient THz generation because even negligible depletion of the pump energy can be accompanied by a high degree of photon-conversion and hence modification of the pump spectrum. Other complicating factors are the presence of self-focusing and self-phase modulation that modify the pump laser and may adversely affect the down-conversion process. The low efficiencies of THz generation also mean that even non-phase-matched parasitic nonlinear conversion processes such as second harmonic generation, can have a significant impact. Finally, perhaps the most critical effect is damage of the nonlinear medium. For $LiNbO_3$ in particular, the traditional laser-induced damage mechanisms, which have known intensity and fluence scaling, is accompanied by processes such as the photo-refractive effect which are strongly affected by factors such as temperature and repetition rate and can cause complex, long-lived changes to the material. In the face of these complexities, a global optimization of the THz generation process, which requires a highly systematic process of varying relevant parameters and performing detailed, quantitative comparisons between experiment, theory and simulation to validate our understanding of the mechanisms at play, has not been done. Multicycle THz generation thus remains in a quasi-infancy and perhaps not surprisingly, considering the difficulty in capturing the full scope of relevant physics, quantitative comparisons between experiment and simulation/theory for the THz yield are practically nonexistent in the literature.

Simulations of efficient narrowband THz generation point to an optimal configuration in which the optical pump is composed of a series of narrow spectral lines separated by the THz frequency [19]. By applying this principle to high-power, Ti:Sapphire laser drivers, new records in narrowband THz-pulse energy have been achieved [9,10]. In these experiments, chirping of the broadband pulses was used to narrow the "instantaneous" spectral content, and pairs of pulses with a delay were combined to produce an effective 2-line spectrum, taking advantage of the time-frequency mapping. This approach, however, suffers from challenges in controlling the constancy (within the duration of the pulse) of the frequency separation between the two lines associated with third order and higher spectral phase inherent to chirped-pulse amplifier (CPA)

Optics EXPRESS

based laser systems [9,22]. Concomitantly, despite the record energies achieved, the conversion efficiencies demonstrated only reached up to 0.24%. Later experiments improved this efficiency to a record 0.89%, which remains the highest reported so far, by developing a customized laser system designed to produce two narrowband spectral lines by combining, temporally chopping and amplifying a pair of single-frequency continuous wave (CW) sources [23]. Increasing the number of spectral lines beyond two is predicted to lead to higher efficiencies, however, maintaining coherence while combining larger numbers of single-frequency sources into a single laser system leads to a considerable increase in complexity, motivating alternative approaches for increasing the number of lines in the spectrum.

Here we pursue an approach based on a time-domain interpretation of the multi-line concept. In the time domain, two spectral lines produce a sinusoidal modulation while greater numbers of lines lead to a steepening of these modulations into distinct pulses in a regular train. We therefore employ an optical setup, based on a sequence of Michelson interferometers, to divide a single short pulse into a high-frequency burst of pulses with a periodicity matching the targeted radiation frequency (~350 GHz). Our setup, together with a customized amplification system, provides tunability over the energy, duration, number and periodicity of the pulses in the train enabling a thorough exploration of parameter space aimed at determining the limits of the nonlinear conversion process. Scans of the pulse-train periodicity are also used to map out the frequency response of our PPLN devices with unprecedented precision, providing a new capability for characterizing essential material properties, such as refractive index and absorption coefficient, under actual experimental conditions. The experimental results are accompanied by a complete set of simulations allowing quantitative comparison and validation of the model. Our results confirm several analytic predictions which, together with assumptions on boundary conditions imposed by material damage, point to specific strategies for optimization of conversion efficiency. We find, in addition, that the agreement between simulation and experiment varies significantly with the choice of parameters, providing evidence for inadequacies in the current model. We discuss perspectives on both the strategies for optimization and the additional physics that may be needed to improve the model.

## 2. Experimental setup

The laser system used was designed from bottom up to produce pulse trains with the desired properties (Fig. 1(a)). It consists of a fiber-based front-end, a pulse divider setup and a chain of home-built amplifiers together with the appropriate dispersion control. The front end, consisting of a home-made fiber oscillator and several fiber amplifiers, produces broad-band laser pulses with an average power of 400 mW and a repetition rate of 40 MHz. The spectrum of the pulses is roughly Gaussian in profile and centered at 1034 nm with a full-width-half-maximum (FWHM) bandwidth of 12 nm.

### *2.1. Pulse divider*

The pulse train is realized by a series of eight polarization-based Michelson interferometers that each produce two copies of its input with the appropriate delay (Fig. 1(b)). Figure 1(c) shows details of an individual interferometer or "divider stage". The incident beam passes through a half-wave plate (HWP) which, together with a polarizing beam splitter (PBS), splits the beam into the two arms. The double-pass through quarter wave plates installed in each arm induces a 90-degree polarization rotation that ensures both beams recombine onto a common output path and minimizes the amount of energy returning along the input line. The waveplates (zero-order air-spaced doublets) and polarizers are anti-reflection coated for 1030 nm to minimize generation of undesired pre- and post-pulses. The pulse in one arm is delayed relative to the other arm by an amount that doubles from divider to divider using a high-precision translation stage. The translation stages are actuated by Physik-Instrumente L-220.20DG linear actuators, enabling

Optics EXPRESS

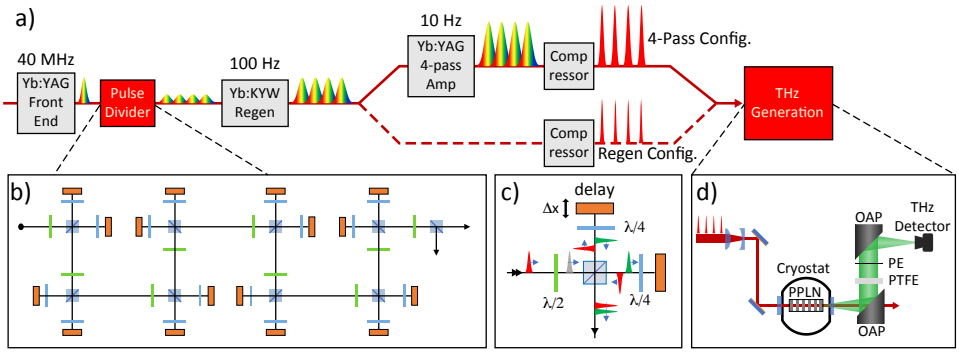


**Fig. 1.** Experimental setup. (a) Conceptual layout of the custom laser system. (b) Schematic layout of the pulse divider for generating up to 256 pulses. (c) Detail of a divider module. A half-wave plate rotates the polarization before the polarizing beam-splitter cube and controls the energy splitting between the two interferometer arms. Quarter wave plates in each arm induce a 90° rotation of the polarization, ensuring the pulses exit the interferometer in the correct direction with high efficiency. Red (green) pulses are vertically (horizontally)-polarized, meaning s(p)-polarized with respect to the polarizer. Grey pulses are polarized at ±45°. (d) Schematic layout of the THz generation and detection.

sub-micron positioning of the pulses as well as automated control over the pulse-train periodicity. Motorization of the HWPs was also implemented in order to ensure precise balancing of the two arms (and thus evenness of the pulse amplitudes) as well as to allow particular divider stages to be effectively by-passed for control of the pulse-train number. The resulting output of the pulse-divider system was a regular train of $2^{N_{Stages}}$ pulses where $N_{Stages} \leq 8$ is the number of active divider stages.

### 2.2. *Pulse train amplification and dispersion control*

The output of the pulse divider was used to seed a room-temperature Yb:KYW regenerative amplifier (regen) which increased the burst energy from roughly 1.5 nJ to a maximum of 3 mJ at a repetition rate of 100 Hz. The output of the regen was then optionally injected into a room-temperature Yb:YAG 4-pass amplifier operating at 10 Hz to increase the burst energy up to a maximum of 20 mJ. Due to differences between the amplification bandwidths of the regen and final 4-pass amplifiers, an interference-based bandpass filter placed before the regen was used with angle tuning to control the long-wavelength cutoff of the spectrum, resulting in a 4 nm output centered at 1028 nm. Due to gain narrowing, the bandwidth after amplification in the 4-pass was further reduced to 1.9 nm. To minimize the peak intensities in the amplifiers and thus maximize the achievable energy, the dispersion is managed in several steps with the objective of filling the space between the pulses as much as possible while avoiding significant overlap between neighboring pulses which produce interference spikes. For this purpose, the dispersion of the pulses is adjusted before the pulse divider to 1.2 ps/nm. A grating compressor installed after the amplifier chain was used to compensate the chirp of the pulses in the train and control the pulse duration. Additional control over the pulse duration was achieved by selecting between two modes of operation, one that included the final 4-pass amplifier ("4-pass configuration", top branch of Fig. 1(a)), providing higher energy pulses with narrower bandwidths, and one that by-passed it, relying for amplification only on the regenerative amplifier, ("Regen configuration", bottom branch of Fig. 1(a)), resulting in broader bandwidth pulses at lower energy.

Optics EXPRESS

### 2.3. THz generation and detection

The compressed pulse train is sent into a commercial PPLN crystal with a poling period of 330 µm. The crystal with dimensions $4 \times 4 \times 20$ mm is cooled to cryogenic temperature (78 K) to minimize THz absorption. Figure 1(d) shows a schematic of the setup. The diameter of the pump beam on the crystal is varied from 1 mm – 1.5 mm (intensity $1/e^2$ radius, $w_0$). The THz radiation is generated colinearly with the laser beam and afterwards is collected and focused onto a THz detector (Gentec SDX-1152) by a pair of 2-inch off-axis parabolas (OAPs) to measure the THz energy. The first OAP features a through-hole allowing investigation of the pump beam after THz generation. Residual IR light from the pump is blocked in front of the crystal with a 10 mm thick Teflon plate and a 2-mm Polyethylene (PE) plate. To avoid optically-induced damage to the PPLN crystal, the incident pulse train peak fluence was limited to below 200 mJ/cm$^2$. To quantify the THz yield, the "internal" conversion efficiency (CE), i.e., the ratio of THz to optical pulse energy within the crystal, is used. This metric allows evaluation of the performance of the THz generation process decoupled from practical issues associated with output coupling and transport of THz radiation. For the calibration of the THz energy inside the crystal we consider the THz losses, including both Fresnel reflections as well as absorption, from all components between the inside of the PPLN crystal and the detector, leading to a total transmission of 19.6% (Table 1). We also consider the Fresnel losses for the laser at the uncoated crystal surface which results in an IR pump transmission of 86.6%. The Fresnel losses were calculated analytically based on indices of refraction, whereas for the fused silica window and the Teflon and PE plate, the transmission was measured. Finally, for the OAPs, the collection efficiency was calculated based on the measured THz beam distribution.

**Table 1. Transmission of THz through elements inducing energy loss between the point just inside the PPLN surface and the detector**

| Element | Transmittance |
|---|---|
| PPLN exit surface | 56% |
| fused silica window | 65% |
| 1 cm Teflon block | 83% |
| 2 mm PE plate | 73% |
| Off-axis parabolas | 89% |
| Total | 19.6% |

## 3. Results and discussion

The experimental parameters that were investigated were the frequency, energy, number, duration, bandwidth and mode-size of the pulses in the train. The experiments were performed in two formats, scanning of the pulse-train frequency, which refers to the periodicity of the pulses in the burst, and scanning of the pulse train energy, which refers to the total energy of the burst.

### 3.1. Analytic treatment

In order to guide the interpretation of our results, we present an analytical derivation of the THz radiation in the undepleted pump approximation. Following the approach which has been presented in [9,21,23,24], the shape of the THz intensity spectrum can be decomposed into two essential contributions, one coming from the properties of the PPLN crystal, and the other from

Optics EXPRESS

the properties of the optical drive laser:

$$I_{THz}(r,\Omega,L) = \pi\varepsilon_0 cn(\Omega)\Omega^2 \mathfrak{T}_{PPLN}(\Omega,\ L) \times \mathfrak{T}_{opt}(r,\Omega). \tag{1}$$

The term describing the crystal contribution is given by $\mathfrak{T}_{PPLN}(\Omega,\ L) = \chi_{eff}^{(2)^2} L^2 g_{PPLN}(\Omega, L)$, where $\chi_{eff}^{(2)}$ is the second order effective nonlinear susceptibility, $L$ is the crystal length and

$$g_{PPLN}(\Omega,\ L) \equiv \frac{1}{\frac{1}{4}\alpha^2(\Omega)L^2 + \Delta k^2(\Omega)L^2}\left[\left(1 - e^{-\frac{\alpha(\Omega)L}{2}}\right)^2 + 4e^{-\frac{\alpha(\Omega)L}{2}}\sin^2\left(\frac{\Delta k(\Omega)L}{2}\right)\right], \tag{2}$$

is a function with maximum value of unity that describes the normalized phase-matching spectrum, $\alpha(\Omega)$ is the THz absorption coefficient and $\Delta k(\Omega)$ is the phase mismatch. The phase mismatch is given by $\Delta k(\Omega) = \frac{2\pi}{\Lambda_{PPLN}}\left(\frac{\Omega-\Omega_{PM}}{\Omega_{PM}}\right)$, where $\Lambda_{PPLN}$ is the poling period of the PPLN, $\Omega_{PM} \equiv \frac{2\pi c}{\Lambda_{PPLN}}(n(\Omega) - n_g(\omega))^{-1}$ is the phase-matched THz angular frequency, $c$ is the speed of light, $n(\Omega)$ is the THz refractive index, $n_g(\omega) \equiv \frac{c}{v_g(\omega)}$ is the optical group index and $v_g(\omega)$ is the optical group velocity. To understand the behavior of this function, it is helpful to look at two extremes. In the first case, we assume a negligible absorption, $\alpha \approx 0$. For this case, we obtain the well-known sinc-squared function:

$$g_{PPLN}(\Omega,\ L) = \mathrm{sinc}^2\left(\pi N_{PPLN}\frac{\Omega - \Omega_{PM}}{\Omega_{PM}}\right), \tag{3}$$

where $N_{PPLN}$ is the number of poling periods, leading to a FWHM relative bandwidth of $\Delta\Omega_{FWHM}/\Omega_{PM} \approx 0.89/N_{PPLN}$. For the experiments performed here, the 20 mm crystal length and the 330 µm period correspond to $N_{PPLN} \approx 61$, leading to a bandwidth of $\Delta\Omega_{FWHM}/\Omega_{PM} = 1.4\%$. On the other extreme if we assume a large absorption, i.e., $\alpha L \gg 1$, such as for $LiNbO_3$ at room temperature, we obtain:

$$g_{PPLN}(\Omega,\ L) \cong \frac{1}{\frac{1}{4}\alpha^2(\Omega)L^2 + \left(2\pi N_{PPLN}\frac{\Omega-\Omega_{PM}}{\Omega_{PM}}\right)^2}, \tag{4}$$

which has a relative FWHM bandwidth of $\Delta\Omega_{FWHM}/\Omega_{PM} \approx \alpha L/2\pi N_{PPLN}$. This result shows that absorption becomes the dominant factor determining the phase-matching bandwidth when $\alpha L/2\pi$>0.89. At cryogenic temperatures (80 K) and for 350 GHz, the absorption coefficient is $\alpha_{80K} \approx 0.8\ \mathrm{cm}^{-1}$, leading to a FWHM bandwidth of $\Delta\Omega_{FWHM}/\Omega_{PM} \approx 0.4\%$, whereas at room temperature (300 K), the absorption coefficient is $\alpha_{300K} \approx 6.7\ \mathrm{cm}^{-1}$, leading to a FWHM bandwidth of $\Delta\Omega_{FWHM}/\Omega_{PM} \approx 3.5\%$.

The second term in Eq. (1), which describes the THz-excitation spectrum associated with the optical driver, is given by:

$$\mathfrak{T}_{opt}(r,\Omega) \equiv \left|\int_0^\infty A_{opt}(r,\omega+\Omega)A_{opt}^*(r,\omega)d\omega\right|^2 = \left|\frac{\mathcal{F}_{t\to\Omega}\{I_{opt}(r,t)\}}{\pi\varepsilon_0 cn(\omega)}\right|^2, \tag{5}$$

where $A_{opt}(\omega)$ is the component of the optical field at optical angular frequency $\omega$ and $\mathcal{F}_{t\to\Omega}\{.\}$ corresponds to the Fourier transform between the time ($t$), and angular frequency ($\Omega$), domains. This expression shows that to first order the key factor in optimizing the optical driver is the shape of the intensity temporal envelope [19]. This fact has important ramifications. First, it implies that two pulses with the same temporal profile but different spectral profiles (e.g., a compressed narrowband pulse and a chirped broadband pulse) should perform equally well. This conclusion,

Optics EXPRESS

of course, ignores higher-order effects such as the dispersion in the optical group velocity which can affect the phase matching. Second, Eq. (5) implies that the temporal positioning of the pulses in the train does not need to be precise on an optical wavelength scale, but only on the scale of the THz wavelength, which is orders of magnitude larger. Therefore, temporal jitter on the femtosecond timescale between the pulses of the train, which is a natural consequence of producing the pulse train with a sequence of non-stabilized interferometers, has relatively little effect on the efficiency of the nonlinear down-conversion process. By comparison, even a sub-femtosecond level of temporal jitter has a dramatic impact on the optical spectrum of the pulse train due to variations in the phase of the interference patterns between the various pairings of pulses in the train. The association of the pulse train with a multi-line optical spectrum is therefore only valid for a perfect pulse train with exact temporal spacing. Nevertheless, for a well-tuned pulse train, (i.e., regular on the scale of the THz period) the optical term $\mathfrak{T}_{opt}(\Omega)$ will have a narrow spectrum centered at the pulse train frequency, $f_{train}$ with a bandwidth that is inversely proportional to the number of pulses, $N_{train}$. To be more precise, we assume a train of Gaussian pulses of the form:

$$I_{opt}(r,t) = \sum_{n=0}^{N_{train}-1} I(r) e^{-\left(\frac{t-t_n}{\Delta t}\right)^2} \tag{6}$$

where $I(r) = I_0 e^{-\left(\frac{r}{\Delta r}\right)^2}$ is the radial intensity profile, $t_n = n/f_{train}$ is the temporal location of the n$^{\text{th}}$ pulse and $\Delta t$ is the $1/e$ duration of an individual pulse. $\mathfrak{T}_{opt}(\Omega)$ then can be written:

$$\mathfrak{T}_{opt}(r,\Omega) \approx \frac{1}{2}\left(\frac{I(r)\Delta t N_{train}}{\pi\varepsilon_0 c n(\omega)}\right)^2 g_{opt}(\Omega) \tag{7}$$

where

$$g_{opt}(\Omega) \equiv e^{-\frac{1}{2}(\Omega\Delta t)^2} \sum_{n=0}^{\infty} \mathrm{sinc}^2\left(\pi N_{train}\frac{\Omega - n\Omega_{train}}{\Omega_{train}}\right) \tag{8}$$

is a function with a maximum value of unity that describes the THz-excitation spectrum of the optical driver, and $\Omega_{train} \equiv 2\pi f_{train}$. The exponential term describes the excitation spectrum attributable to an individual pulse, while the sinc-squared terms describe the contribution from the pulse train in the form of a harmonic series. As will be discussed further below, for the pulse-durations used in our experiments, the only significant contribution to the THz generation comes from the first ($n = 1$) harmonic. For the remainder of the analytic treatment, we therefore keep only the term $g^{(1)}_{opt}(\Omega) \equiv e^{-\frac{1}{2}(\Omega\Delta t)^2}\mathrm{sinc}^2\left(\pi N_{train}\frac{\Omega-\Omega_{train}}{\Omega_{train}}\right)$. Since we allow for the pulses being linearly chirped, we note that $\Delta t$ represents the chirped-pulse duration (not the transform-limited one) and thus satisfies $\Delta t = 1/\Delta\omega_{slice}$, where $\Delta\omega_{slice}$ is the $1/e$ width of the optical-intensity spectrum at an instantaneous temporal slice of an individual pulse. For fully compressed pulses, $\Delta\omega_{slice} = \Delta\omega$, where $\Delta\omega$ represents the integrated optical-intensity spectrum. We can therefore see that the exponential term describes the impact on the conversion efficiency of the slice optical bandwidth (which is connected to the presence of temporal-intensity gradients). This picture is consistent with the insight provided by Eq. (5).

The FWHM relative bandwidth of the THz-excitation spectrum is $\Delta\Omega_{FWHM}/\Omega_{train} \approx 0.89/N_{train}$. The pulse divider was operated using $N_{Stages} = 5 - 8$ stages, yielding $32 \le N_{train} \le 256$ and optical-excitation relative bandwidths in the range $0.3\% \le \Delta\Omega_{FWHM}/\Omega_{train} \le 2.8\%$. The conversion efficiency, averaged over the radial dimension is then given by:

$$\eta_{THz}(L) = \frac{\int_{-\infty}^{\infty}\int_{0}^{\infty} I_{THz}(r,\Omega,L)2\pi r dr d\Omega}{\int_{-\infty}^{\infty}\int_{0}^{\infty} I_{opt}(r,t)2\pi r dr dt} \tag{9}$$

Optics EXPRESS

which becomes:

$$\eta_{THz}(L) = \frac{F_0 {\chi_0^{(2)}}^2 L^2}{\pi^2 \varepsilon_0 c^3 n^2(\omega)} \int_{-\infty}^{\infty} \frac{\Omega^2}{n(\Omega)} g_{PPLN}(\Omega, L) \times g_{opt}^{(1)}(\Omega) d\Omega \tag{10}$$

where $F_0 \equiv \sqrt{\pi} I_0 \Delta t N_{train}$ is the peak fluence of the optical beam (i.e., the peak fluence integrated over all pulses in the train).

### 3.2. Characterization of the pulse train

We performed a detailed analysis of the pulse train's temporal-intensity structure (Fig. 2) to evaluate the functionality of the pulse divider and determine how well the output compares to the desired structure. Key parameters of interest are the regularity of the pulse spacing, the uniformity of the pulse amplitudes and the pulse duration relative to the period. To measure the temporal-intensity structure, the output of the pulse divider was compressed and combined with a background-free geometry in a type II BBO crystal with a single probe pulse picked off before the pulse divider. By scanning the delay of the probe pulse and monitoring the sum-frequency yield, a second-order cross-correlation between the probe and the pulse train was obtained. The results for a complete 256-pulse train are presented in Fig. 2(a). While some variation in the amplitude of the train is evident, the figure shows that a highly-periodic structure was produced. To quantify the degree of periodicity in the pulse train, we calculated the Fourier transform (FT) of the temporal-intensity structure and normalized it to the amplitude of the "DC" peak at zero frequency (Fig. 2(b)). The normalized FT, which directly corresponds to the function $g_{opt}(\Omega)$, features a strong and very sharp "fundamental" peak at 347.1 GHz, with an amplitude of 20% (relative to the DC peak), a second-harmonic peak at 694.1 GHz with a relative amplitude of 2%, and very little amplitude at other frequencies. The fact that most of the spectrum is concentrated into a single narrow side-peak confirms that the pulse train is highly periodic. The presence of the second harmonic peak and its amplitude relative to the fundamental also match well with the prediction (based on Eq. (8)), further confirming the regularity of the train.

As highlighted by Fig. 2(c) a large number of additional peaks are also present across the spectrum, but at a very low amplitude. These peaks likely come from a variety of sources, including "ghost" pulses reflecting from the surfaces of transmissive optics in the pulse divider (e.g., waveplates and polarizers), of which there are many. The transmission through the pulse divider was measured to be approximately 90%, half of which was split into each output port of the final polarizer. Considering a total of 144 surfaces (including all waveplates, polarizers and mirrors), the average loss per surface was therefore ~0.03%. Any ghost pulses would therefore be on this level of intensity. Despite this low level, the repeated interaction with optics of a consistent internal structure (e.g., the air-spaced, zero-order waveplates), could accumulate, resulting in more prominent peaks in the FT. However, aside from stealing a small amount of energy from the main side peak, these other peaks are not expected to affect the THz generation process since they lie outside of the crystal's phase-matching spectrum delineated by the filled blue areas in Figs. 2(b) and 2(c). Their contributions are thus effectively filtered out.

We next evaluate how variations in the amplitude, spacing and duration of the pulses in the train (as measured by the cross-correlation) impact the structure of the FT. We first performed Gaussian fits to each of the peaks in the cross-correlation in Fig. 2(a) to determine the amplitudes, temporal locations and temporal widths of each peak. Figure 2(d) shows a close up of a section of the measured cross-correlation, with the Gaussian fits depicted by the red-filled regions. The fits indicate that the amplitude varied by 29% (std. dev.), the pulse spacing varied by 8% and the pulse duration varied by 18%. The fit information was then used to numerically re-create the pulse train under different assumptions in order to independently evaluate the effect of the three types of variation on the height and width of the fundamental peak in the FT. An ideal pulse train

Optics EXPRESS

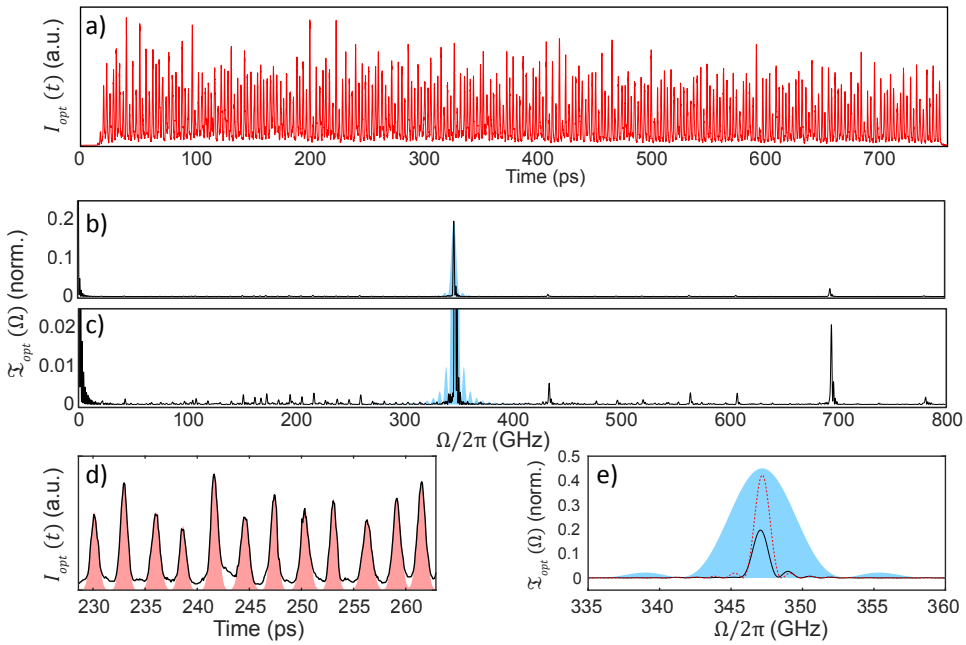


**Fig. 2.** Analysis of pulse-train temporal structure. (a) Measurement of the temporal-intensity structure of a 256-pulse train extracted and compressed before the regen amplifier. The measurement was done by second-harmonic cross-correlation with an individual compressed pulse extracted before the pulse divider. (b) Fourier transform of the data in (a), solid black line, together with the calculated phase-matching spectrum of the PPLN, depicted by the blue-filled region. (c) Same as (b), but zooming in on the y-scale to highlight the low-intensity peaks. (d) Close-up of a section of the measurement in (a), solid black line, together with Gaussian fits to the peaks, depicted by the red-filled regions, used to quantify the variation in parameters of the pulses in the train. (e) Close-up of the fundamental peak in (b), solid black line, together with a calculation of the fundamental peak for an ideal, perfectly regular pulse train with the same average pulse spacing and pulse duration, dotted red line. The blue-filled region depicts the calculated phase-matching spectrum of the PPLN crystal scaled for convenient comparison to the other traces.

(i.e., uniform amplitudes, temporal spacing and duration) was first created as a reference using the average values of the measured temporal spacing and FWHM width of the cross-correlation peaks, i.e., 2.88 ps and 1.0 ps, respectively. For this ideal case, the height of the fundamental peak was 0.42 (relative to the DC peak) and the FWHM width was 1.2 GHz. Including only the 29% variation in the pulse amplitudes resulted in no noticeable change to the height of the FT side peak, but did result in a low-level of noise across the spectrum. Including only the 18% variation in pulse duration lowered the FT side peak height by 5% to 0.40. Finally, including only the 8% variation in pulse spacing lowered the fundamental peak height by 17% to 0.34. In all cases, the FWHM width of the fundamental peak remained at 1.2 GHz which corresponds to a relative bandwidth of 0.35%, in exact agreement with analytic predictions based on Eq. (8). The pulse spacing regularity is thus (as to be expected) a primary factor determining the height of the fundamental peak, with pulse duration and amplitude variations playing a relatively small role. Figure 2(e) shows a comparison of the FT side peaks from the measured cross-correlation (black solid line) and from the recreated ideal case (red dotted line), with the phase-matching spectrum (blue-filled region), which has a > 4x larger relative bandwidth of 5.1 GHz, for context.

Optics EXPRESS

As clarified by the analytical treatment above, the structure of the FT (i.e., the function $g_{opt}(\Omega)$) determines the effectiveness of the pulse train for driving THz generation in the PPLN crystal. Figure 2(e) highlights that the pulse train produced was of sufficient regularity and quality to produce a fundamental peak in the FT with a height close to 50% of the maximum possible and a width narrower than the phase-matching spectrum of the PPLN in line with analytical expectations. It should be noted that a significant fraction of the measured variability comes from the cross-correlation measurement process itself which required about eight hours to perform. The measurement error can be evaluated by considering the constraints to the pulse-parameter variations intrinsic to the design of the pulse divider. First, as the pulse divider is a passive optical device, it cannot create variations in the pulse duration, since all pulses experienced the same dispersion. Second, since each divider stage produces a pair of copies of the train it receives, the temporal structure of each copy must be identical to within an overall amplitude difference. A detailed comparison of the first and second halves of the cross-correlation (not shown), however, revealed noticeable discrepancies in both the pattern of amplitudes and the pattern of pulse spacings which can only be attributed to the measurement. The actual pulse train was therefore *more regular* than indicated by the variation figures and FT analysis above. Quantifying and correcting for these measurement errors is straight forward and will be the subject of future refinements of the technique.

Finally, we evaluate the resultant pulse train in the context of the goal mentioned in the introduction to increase the steepness of the temporal modulation beyond what can be done with the two-spectral-line concept. First, as is evident in Figs. 2(a) and 2(d), the pulse divider was successful in creating a train of pulses that were highly distinct. The average contrast between the peaks and values of the temporal-intensity modulation was very high at about 87%. Assuming Gaussian pulses and accounting for the square-root-of-2 factor between an auto-correlation and the actual intensity profile, the pulses in the measured train had an average FWHM pulse duration of 0.71 ps, meaning that the ratio between the pulse duration and the train period was over 4:1, which is at least twice as good as the 2:1 produced by the interference of two spectral lines. We thus conclude that the pulse-divider approach is highly effective for producing the desired pump temporal-intensity structure.

### 3.3. Measurement of the crystal index and absorption

A major advantage of the pulse-divider approach is the ability to precisely map out the THz efficiency as a function of pulse-train frequency, $f_{train}$. The shape of the resultant function $\eta_{THz}(\Omega_{train})$, which we henceforth refer to as the "tuning curve", provides information about the phase-matching spectrum, $g_{PPLN}(\Omega, L)$, for an individual PPLN crystal which can be used to determine the values of key material properties, such as the THz refractive index, $n(\Omega_{PM})$, and the THz absorption coefficient, $\alpha(\Omega_{PM})$. Although such parameters *can* be measured off-line using devices like time-domain spectrometers, our approach has the distinction of being done in situ under the actual conditions of THz generation and therefore provides a more direct characterization of the nonlinear interaction. To understand how the material properties can be recovered, we examine Eq. (10) more carefully. As shown above, the functions $g_{PPLN}(\Omega, L)$ and $g^{(1)}_{opt}(\Omega)$ are narrow, with relative bandwidths of at most a few percent. We can therefore approximate that other terms which vary slowly with frequency, such as $n(\Omega)$, $\alpha(\Omega)$, $\Omega^2$ and $e^{-\frac{1}{2}(\Omega\Delta t)^2}$ are effectively constant. The conversion efficiency, which we use as our THz signal then simplifies to:

$$\eta_{THz}(\Omega_{train}) \approx \frac{F_0 {\chi^{(2)}_0}^2 L^2 \Omega^2_{PM}}{\pi^2 \varepsilon_0 c^3 n^2(\omega) n(\Omega_{PM})} e^{-\frac{1}{2}(\Omega_{PM}\Delta t)^2} \int_{-\infty}^{\infty} g_{PPLN}(\Omega, L) \times \mathrm{sinc}^2 \left[ \pi N_{train} \frac{\Omega - \Omega_{train}}{\Omega_{train}} \right] d\Omega \tag{11}$$

Optics EXPRESS

This expression shows that the tuning curve is essentially the convolution between the phase-matching spectrum of the crystal and the THz excitation spectrum of the laser. Measuring $\eta_{THz}(\Omega_{train})$ and $g^{(1)}_{opt}(\Omega)$ therefore, in principle, allows reconstruction of $g_{PPLN}(\Omega, L)$. Here we extract the material parameters of our PPLN crystal by numerically calculating the tuning curve based on Eq. (11) and varying the parameters $n(\Omega_{PM})$ and $\alpha(\Omega_{PM})$ to optimize the fit with the data. The results of this analysis for a 128-pulse train are presented in Fig. 3. The measured tuning curve is shown in Fig. 3(a) (blue dots) together with a calculation using $n(\Omega_{PM}) = 4.8899$ and $\alpha(\Omega_{PM}) = 0.76$ cm$^{-1}$ from literature [25] (red-filled region), and a calculation using the best-fit values $n(\Omega_{PM}) = 4.8325$ and $\alpha(\Omega_{PM}) = 0.50$ cm$^{-1}$ from our optimization (black, solid line). The match to the data for the best-fit case is remarkably good, confirming the conclusion from the analysis of Fig. 2 that the pulse train is highly regular. Due to the narrowness of the tuning curve, the shift of the peak between the measured tuning curve ($\Omega^{meas}_{PM}/2\pi = 347.1$ GHz) and the calculated one using the literature value of the index ($\Omega^{lit}_{PM}/2\pi = 339.7$ GHz) is quite clear, despite the difference in THz index, which defines this frequency, only being about 1%.

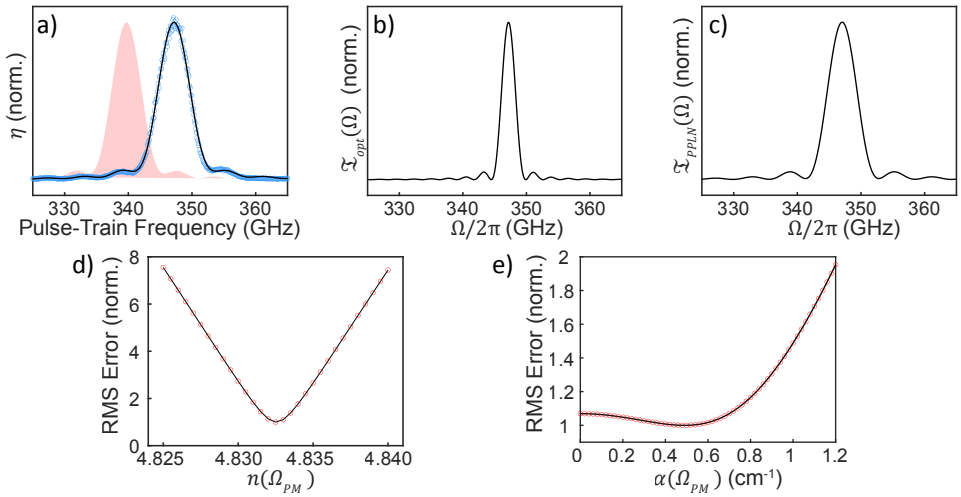


**Fig. 3.** Analysis of tuning curve for determining THz index and absorption coefficients. (a) Measured tuning curve (blue dots) compared with the calculated tuning curve (from Eq. (11)) using literature values of the index and absorption (red-filled region) and the calculated tuning curve using the best-fit values of index and absorption (black line). (b) THz-excitation spectrum, $g^{(1)}_{opt}(\Omega)$, calculated using Eq. (8) for $\Omega_{train} = \Omega_{PM}$. (c) Phase-matching spectrum calculated using Eq. (2) and the best-fit values of index and absorption, $n(\Omega_{PM}) = 4.8325$ and $\alpha(\Omega_{PM}) = 0.50$ cm$^{-1}$, respectively. (d) RMS error between the measured and calculated tuning curves as a function of the THz index, normalized to the minimum value. (e) RMS error between the measured and calculated tuning curves as a function of the THz absorption coefficient, normalized to the minimum value.

The THz-excitation spectrum and the phase-matching spectrum used for the optimization are shown in Fig. 3(b) and 3(c), respectively, plotted for the optimized values of the index and absorption, and for $\Omega_{train} = \Omega_{PM}$. The optimization was done by minimizing the root-mean square (RMS) difference or "error" between the measured and calculated tuning curves. The dependence of the RMS error (normalized to the minimum value) on $n(\Omega_{PM})$ is plotted in Fig. 3(d). The plot shows that the RMS error is highly sensitive to the THz index, with a 7-fold change in error caused by an 0.16% change in the index. This result indicates that, in principle, variations in index down to the 3$^{rd}$ digit after the decimal point are resolvable. It must be noted, however, that shifts in the peak of the tuning curve can also be caused by errors in measurement

Optics EXPRESS

of the pulse-train frequency or in the poling period of the PPLN. Therefore, a precise, *absolute* determination of the index also requires an equally precise determination of these other parameters which is not trivial. However, this methodology is well-adapted for measuring small relative changes in index caused, e.g., by changes in temperature or by intensity-driven nonlinear effects which are relevant for precise optimization of the THz generation process.

By contrast, as shown by Fig. 3(e), the sensitivity of the error to the absorption coefficient is much less. So, while the best-fit value of $0.50\,\mathrm{cm}^{-1}$ is lower than the expected value of $0.76\,\mathrm{cm}^{-1}$, it is not clear how meaningful this difference is. The lack of sensitivity is expected at cryogenic temperatures since the absorption coefficient is very low and does not strongly affect the phase-matching spectrum of the crystal. As derived in the analytical section above, the effect of absorption becomes strong for $\alpha L/2\pi>0.89$, whereas for our parameters ($L = 2$ cm and $\alpha = 0.76$ cm$^{-1}$), $\alpha L/2\pi = 0.24$. Nevertheless, the increasing steepness of the error curve for larger values of $\alpha$ suggests that $\alpha<1$ cm$^{-1}$ is reliable. These results confirm the validity and benefit of the pulse-train approach as an in-situ probe of the crystal properties. In particular, the spectral resolution is much improved compared to that obtained using the approach described in [23] in which the separation of two spectral lines was scanned. In the previous work, sampling the tuning curve with about 10 points over the $\sim 10$ GHz bandwidth (i.e., a resolution of $\Delta\Omega/2\pi \approx 1$ GHz) required control over and resolution of the optical spectral lines at the level of $\Delta\lambda_{opt} \approx 0.003$ nm which was at the edge of what could be achieved, leading to a noisy reconstruction. By contrast, with the pulse-train approach, the spectral resolution in the measurement of $\eta_{THz}(\Omega_{train})$ was limited by the minimum reliable step size of the delay stages ($\sim$0.1 $\mu$m), which allowed an order-of-magnitude improvement in tuning-curve resolution down to $\Delta\Omega/2\pi \approx 0.07$ GHz.

### 3.4. Performance vs. number of pulses

In this section, we examine the dependence of the THz-generation performance on the number of pulses in the train ($N_{train}$). For the remainder of the article, the THz yield measurements correspond to an optimized pulse train with frequency $\Omega_{train} = \Omega_{PM}$. The "performance" is then defined as the ratio between the efficiency and either the peak fluence or the peak intensity of the pulse-train optical driver. We purposefully ran experiments at sufficiently low fluence and intensity to avoid saturation of the THz generation process and hence remain in a linear regime where we can expect a good agreement with predictions assuming an undepleted pump. Control over the number of pulses was implemented by tuning the energy splitting in each divider stage. When all eight stages have equal splitting between the two arms, 256 pulses are created. To reduce the number of pulses by half, the energy splitting in the last stage is adjusted, using the associated half wave plate, to send the energy exclusively into one arm. To ensure the absence of low-level ghost pulses, the unused arm was also blocked. By continuing this process, the number of pulses can be reduced by the desired powers of 2, so that $N_{train} = 2^{N_{stages}}$, where $N_{stages}$ is the number of "active" stages for which the energy is split between the two arms. By successively activating or deactivating the last stage in the series, we ensured that the periodicity of the train was not affected but only the number of pulses in the pulse train. The conversion efficiency (CE) of THz generation was measured as function of the pump fluence, $F_0$, for $N_{stages} = \{5,\ 6,\ 7,\ 8\}$ corresponding to $N_{train} = \{32,\ 64,\ 128,\ 256\}$. The results are shown in Fig. 4 for both the *regen configuration* (Fig. 4(a),(d)) and the *4-pass configuration* (Figs. 4(b),(e)) using fully compressed (near transform-limited) pulses of duration $\Delta t_{FWHM} = 0.54$ ps and $\Delta t_{FWHM} = 0.88$ ps, respectively.

Looking at the graphs of efficiency versus peak fluence (Figs. 4(a),(b)), we see that at a fixed fluence, the conversion efficiency is lower for larger numbers of optical pulses in the train. This behavior seems intuitive since increasing the number of pulses at constant fluence reduces the energy, and hence the intensity, of the individual pulses in the train. We might then expect that at fixed intensity, the conversion efficiency is independent of pulse-train number. However,

Optics EXPRESS

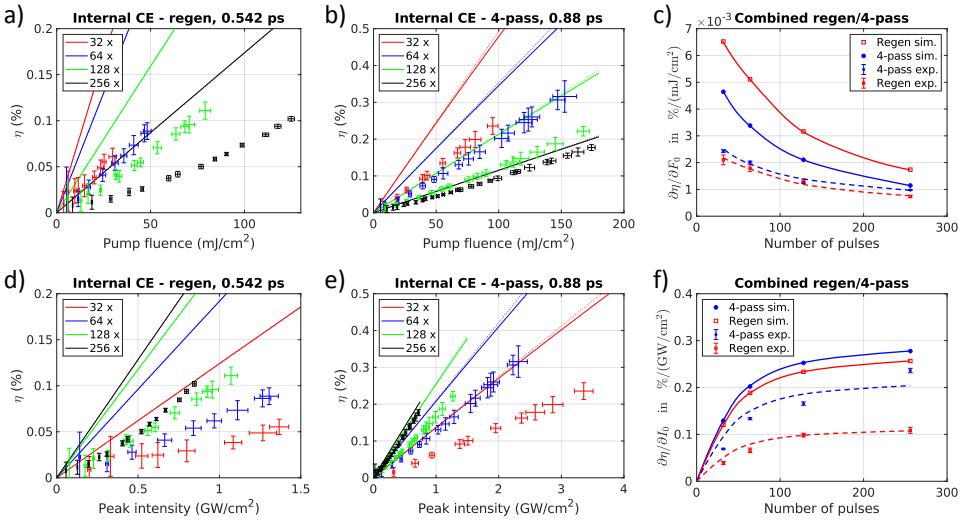


**Fig. 4.** (a) Internal conversion efficiency (CE) as function of the pulse train fluence for different number of pulses (crosses) compared to the corresponding simulation curves (lines) in the *regen configuration* for which the single-pulse duration was 0.542 ps. (b) The same as (a), but for the *4-pass configuration* for which the single-pulse duration was 0.88 ps. (c) The average slope $\partial\eta/\partial F_0$ for each curve and data set in (a) and (b) plotted against the number of pulses in the train. This quantity represents the "fluence-based performance metric". The red and blue points with error bars correspond to best-fit slopes of the regen and 4-pass data in plots (a) and (b), respectively. The red-square and blue-circle markers correspond to the slopes from the regen and 4-pass simulations in (a) and (b), respectively. The solid and dashed lines are guides to the eye. (d) and (e) Same as (a) and (b), but plotted vs. the average peak intensity of the pulses in the train (calculated from the total energy, the number of pulses and the individual pulse duration). (f) The average slope $\partial\eta/\partial I_0$ for each curve and data set in (d) and (e) plotted against the number of pulses in the train. This quantity represents the "intensity-based performance metric". The red and blue points with error bars correspond to best-fit slopes of the regen and 4-pass data in plots (a) and (b), respectively. The red-square and blue-circle markers correspond to the slopes from the regen and 4-pass simulations in (a) and (b), respectively. The solid and dashed lines are guides to the eye.

Figs. 4(d),(e) show, in fact, that at constant intensity the efficiency improves with pulse-train number. To understand these results, we perform both analytical and numerical calculations of the efficiency for each parameter set. The analytical calculations were based on Eq. (11), while the numerical calculations were done using one-dimensional (1D) simulations which included the effects of pump depletion, second harmonic generation (SHG) and self-phase modulation (SPM). In order to account for the transverse intensity variation in the optical beam, 1D simulations were performed for the peak of the beam, and the estimated average efficiency was obtained from the simulated efficiency by dividing by two, which assumes a Gaussian spatial beam profile [19].

The analytical and numerical results, plotted in each graph of Fig. 4, are represented by dashed and solid lines, respectively, of the same color as the corresponding data. In all cases, the analytical and numerical results agree very well with each other (in some cases so well that they overlap), which verifies the validity of the undepleted-pump approximation and the suitability of the analytic description. However, the agreement between the experimental results and either analytical or numerical results depended strongly on the experimental configuration and pulse-train number, varying from a discrepancy of about 10% for 256 pulses in the *4-Pass configuration* to a factor of about 300% for 32 pulses in the *Regen configuration*. In all cases,

Optics EXPRESS

the predicted efficiencies were higher than the measured ones. Despite the discrepancy in magnitude, both the linearity of the curves and the dependence of the slope on pulse-train number match well between experiment and calculation. The comparison is summarized in Fig. 4(c), which shows the fluence-based performance metric $\partial\eta_{THz}/\partial F_0$ as a function of $N_{train}$ and in Fig. 4(f), which shows the intensity-based performance metric $\partial\eta_{THz}/\partial I_0$ as a function of $N_{train}$. Despite the discrepancy in overall magnitude, the functional dependence of the performance on pulse-train number is very similar between calculation and experiment. This dependence can be understood analytically. If we take the case of eight divider stages and 256 pulses, as discussed above, $g^{(1)}_{opt}(\Omega)$ is considerably narrower than $g_{PPLN}(\Omega, L)$. We can then approximate that $g_{PPLN}(\Omega, L) \approx g_{PPLN}(\Omega_{PM}, L) = \left(1 + e^{-\frac{\alpha L}{2}}\right)^2 / \frac{1}{4}\alpha^2 L^2$ is constant and pull it out of the integral in Eqn. (10).

$$\eta_{THz} \approx \frac{F_0 \chi_0^{(2)^2} L^2 \Omega_{PM}^3}{\pi^2 \varepsilon_0 c^3 n^2(\omega) n(\Omega_{PM}) N_{train}} e^{-\frac{1}{2}(\Omega_{PM}\Delta t)^2} g_{PPLN}(\Omega_{PM}, L) \tag{12}$$

This expression shows that the fluence-based performance is inversely related to pulse-train number ($\partial\eta_{THz}/\partial F_0 \propto 1/N_{train}$), which confirms the behavior in Fig. 4(c). Similarly, if we look at the intensity-based performance metric and remember that $F_0 = \sqrt{\pi} I_0 \Delta t N_{train}$, the dependence on pulse-train number disappears and we get $\partial\eta_{THz}/\partial I_0 = const.$, which also aligns with intuition. However, the above analysis was predicated on the assumption that $N_{train} > N_{PPLN}$ in order to consider $g_{PPLN}(\Omega, L)$ as constant. For small values of $N_{train}$, we expect that $g_{PPLN}(\Omega, L)$ will be narrower than $g^{(1)}_{opt}(\Omega)$, and we can then approximate the latter as constant ($g^{(1)}_{opt}(\Omega) \approx e^{-\frac{1}{2}(\Omega_{PM}\Delta t)^2}$):

$$\eta_{THz} \approx \frac{\sqrt{\pi} I_0 \Delta t N_{train} \chi_0^{(2)^2} L^2 \Omega_{PM}^2}{\pi^2 \varepsilon_0 c^3 n^2(\omega) n(\Omega_{PM})} e^{-\frac{1}{2}(\Omega_{PM}\Delta t)^2} \int_{-\infty}^{\infty} g_{PPLN}(\Omega, L) d\Omega \tag{13}$$

from which we find that $\partial\eta_{THz}/\partial I_0 \propto N_{train}$. The intensity-based performance metric therefore should transition from linear at low pulse-train number to flat at high pulse-train number, which is exactly what we see. The implication is that to optimize the efficiency, the pulse-train number should be matched to the crystal, with $N_{train} \geq N_{PPLN}$. For pulse trains with too few pulses, the THz-excitation spectrum is broader than the phase-matching spectrum and is consequently filtered, reducing the efficiency.

### 3.5. Performance vs. pulse duration

In this section, we examine the effect of pulse duration on the performance. Figure 5 and Fig. 6 show the results of pulse-duration studies for $N_{train} = 256$ and $N_{train} = 128$, respectively. Both *4-pass* and *regen configurations* were used. The pulse duration was controlled by adjusting the spacing between the gratings in the compressor after the final amplifier, and hence the chirp of the pulses. The pulse durations were then measured using a commercial autocorrelator. In the *4-pass configuration*, the minimum FWHM pulse duration was 0.71 ps, while for the *regen configuration*, which supported a broader bandwidth, the minimum pulse duration was 0.47 ps. As in Fig. 4, the experimental results for each case are accompanied by analytical and numerical calculations. Let us first consider the results with 256 pulses in Fig. 5. Plotting the efficiency vs. peak fluence for the *regen configuration* (Fig. 5(a)) and the *4-pass configuration* (Fig. 5(b)), we see that the efficiency decreases as the pulse duration increases. Equation (11) shows that the fluence-based performance is described by: $\partial\eta_{THz}/\partial F_0 \propto e^{-\frac{1}{2}(\Omega_{PM}\Delta t)^2}$ which confirms the reduced performance for longer pulses. This expression identifies the effective or "slice" bandwidth as the limiting factor in the efficiency. Longer pulses have reduced temporal gradients, and hence lower slice bandwidths. Figure 5(c) summarizes the behavior of the fluence-based performance with pulse

Optics EXPRESS

duration. Once again, the experimental results are a factor of 2 – 3x lower in magnitude, but the functional dependence on pulse duration is quite similar. And as with the pulse-train-number study, the experiments using the *regen configuration* perform worse than those using *4-pass configuration*.

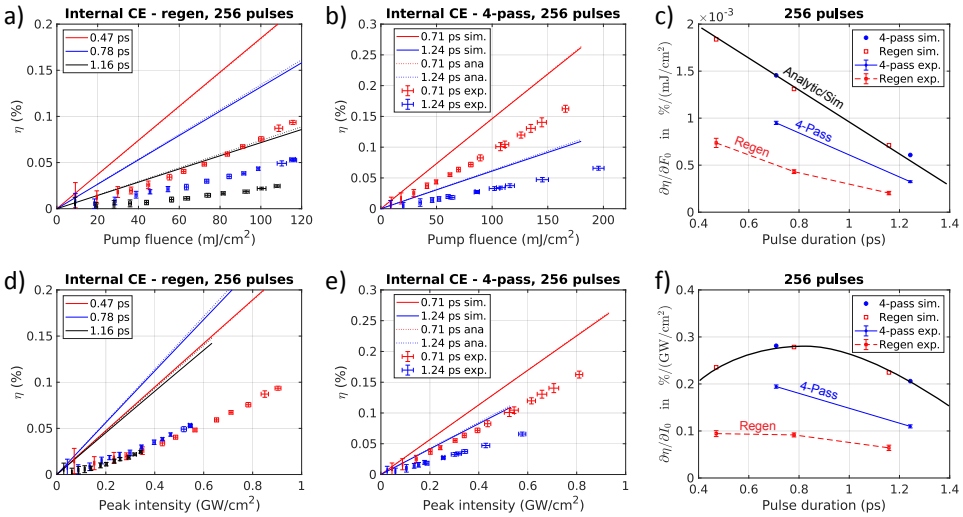


**Fig. 5.** Effect of pulse duration on efficiency for train of 256 pulses. (a) Efficiency vs. pump fluence for three different pulse durations in the *regen configuration*. Data are represented by markers and associated error bars with different colors for each pulse duration. Simulations for each case are represented by solid lines of the same color, while dotted lines of each color represent analytic calculations. The linearity of the simulation and analytic calculations as well as their similarity to each other in value show that the nonlinear process is far from saturation and is well described by the undepleted pump approximation. (b) The same as (a) but for two pulse durations in the 4-pass configuration. (c) Slopes of best-fit lines for the data and simulations in (a) and (b). This graph shows that at fixed fluence the efficiency reduces as pulse duration increases. This trend is to be expected, as increasing the pulse duration at fixed fluence lowers the peak intensity. (d), (e) Same as (a), (b), but plotted as a function of peak intensity. (f) Same as (c), but for the data in (d) and (e). This graph shows that simulation predicts, in accordance with analytic theory, that at fixed intensity there is an optimum pulse duration.

By comparison, at constant intensity (Figs. 5(d),(e)) the conversion efficiency displays a relatively weaker dependence on pulse duration than at constant fluence (Figs. 5(a),(b)). In particular, the *regen-configuration* data is nearly independent of pulse duration. Re-expression of Eq. (11) in terms of intensity shows that the intensity-based performance is described by: $\partial\eta_{THz}/\partial I_0 \propto \Delta t e^{-\frac{1}{2}(\Omega_{PM}\Delta t)^2}$. The extra factor of the pulse-duration, $\Delta t$, for the intensity case indicates an optimum for a particular pulse duration. Setting $\partial\eta_{THz}/\partial I_0 = 0$ results in an optimum of $\Delta t_{optimum} = 1/\Omega_{PM}$, which, for a THz frequency of 347 GHz yields a FWHM duration of ~0.8 ps, as can be seen in Fig. 5(f). This figure shows that the pulse durations we tested were close to the optimum which explains the weak dependence of conversion efficiency. Data from both the *regen* and *4-pass configurations* do show a lower efficiency on the long side of the optimum, in agreement with calculation, and the *Regen-configuration* data shows a barely perceptible peak at 0.78 ps, also in rough agreement with calculation. However, a larger range of pulse-duration values and a smaller step size would clearly be beneficial to more convincingly demonstrate the expected dependence of efficiency on pulse duration. The data obtained with trains of 128 pulses (Fig. 6) show a very similar behavior to those obtained with 256 pulses.

Optics EXPRESS

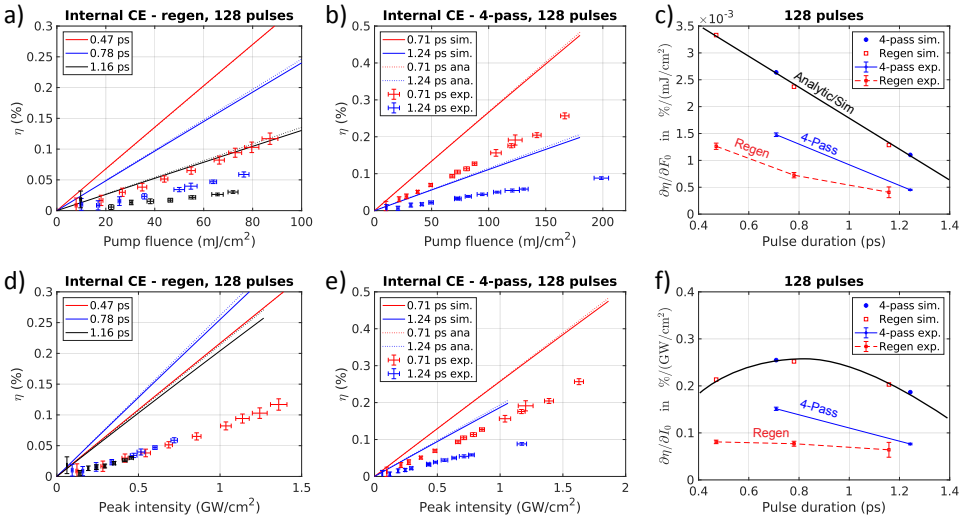


**Fig. 6.** Effect of pulse duration on efficiency for train of 128 pulses. (a) Efficiency vs. pump fluence for three different pulse durations in the *regen configuration*. Data are represented by markers and associated error bars with different colors for each pulse duration. Simulations for each case are represented by solid lines of the same color, while dotted lines of each color represent analytic calculations. The linearity of the simulation and analytic calculations as well as their similarity to each other in value show that the nonlinear process is far from saturation and is well described by the undepleted pump approximation. (b) The same as (a) but for two pulse durations in the 4-pass configuration. (c) Slopes of best-fit lines for the data and simulations in (a) and (b). This graph shows that at fixed fluence the efficiency reduces as pulse duration increases. This trend is to be expected, as increasing the pulse duration at fixed fluence lowers the peak intensity. (d), (e) Same as (a), (b), but plotted as a function of peak intensity. (f) Same as (c), but for the data in (d) and (e). This graph shows that simulation predicts, in accordance with analytic theory, that at fixed intensity there is an optimum pulse duration.

### 3.6. *Effect of beam size on performance*

For laser systems with limited energy, shrinking the beam size in order to achieve the intensities required for efficient nonlinear conversion is a standard approach. For THz generation, however, the ultra-large THz wavelengths and the associated strong divergence represents a unique challenge which places a lower limit on the optical beam size and hence on the pulse energy needed for effective conversion. In this section, we make a preliminary evaluation of the impact of the optical beam size on the performance of the pulse trains for THz generation. Figure 7 shows comparisons of performance for two beam sizes in the *regen configuration*.

For the pulse-train number study (Figs. 7(a),(c)), the "larger beam" had $1/e^2$ radii of $1.27 \times 1.78$ mm$^2$, while the smaller beam had $1/e^2$ radii of $0.92 \times 1.08$ mm$^2$. The figures show that the impact of beam size on the efficiency is considerable, with the ratio of efficiencies matching closely to the ratio of the beam areas. A natural guess is thus that the beam-size sensitivity is connected to diffraction of the THz, which scales quadratically with beam size. For 347 GHz radiation, the wavelength inside the PPLN is 0.18 mm and the corresponding Rayleigh ranges for the larger and smaller beams were therefore 20 mm and 8.8 mm, respectively. Considering the 20 mm length of the PPLN, diffraction is thus a likely candidate to explain the beam-size sensitivity. It should be noted that the pulse duration for the larger beam was 0.54 ps while that of smaller beam was 0.67 ps. However, based on the results in Figs. 5(c),(f) and Figs. 6(c),(f), this difference in pulse

Optics EXPRESS

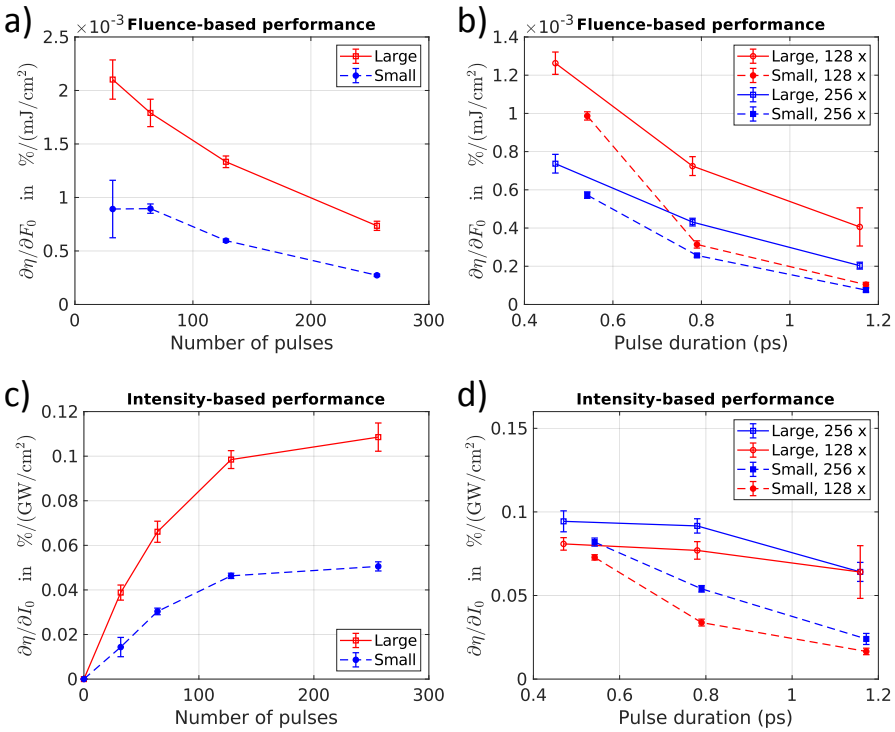


**Fig. 7.** Impact of beam size on efficiency for regen configuration. (a) Fluence-based performance vs. pulse number. (b) Fluence-based performance vs. pulse duration. (c) Intensity-based performance vs. pulse number. (d) Intensity-based performance vs. pulse duration.

duration only had a minimal impact. For the pulse duration study (Figs. 7(b),(d)), the larger beam had the same size as above, but the smaller beam had $1/e^2$ radii of $1.02 \times 1.33$ mm$^2$. Despite a beam-size reduction of only 23%, the impact on the performance was, however, still large.

## 4. Discussion and conclusions

We have presented a novel methodology based on the use of flexible trains of optical pulses for driving THz generation via nonlinear optical down conversion in the narrowband, multicycle regime. The use of high-number pulse trains experimentally addresses a configuration identified by simulation as promising for extending conversion efficiencies into the multiple-percent regime, which would represent a major breakthrough for the field. Here we have taken an important step along this path by performing an experimental investigation of the impact of key parameters on the conversion process and both quantitatively and qualitatively comparing the results with analytical and numerical calculations. In particular we have concentrated on the pulse train frequency, the number of pulses, the pulse duration and the beam size. The dependences of efficiency on pulse-train frequency, pulse number and pulse duration match very well between calculation and experiment, despite disagreements of up to a factor of 2–3 in the magnitude. The beam-size study is also consistent with expectations, but a more thorough experimental study is warranted in which the beam size is varied systematically.

This work helps to emphasize that the topic of agreement between calculation and experiment is not a simple one. As our results show, the closeness of the agreement varies greatly (from factors near unity to factors of several) depending on the parameters of the study. In particular, we find

Optics EXPRESS

that the agreement improves for larger numbers of pulses, shorter pulses and larger beams (Fig. 8). It is tempting to blame discrepancies on the lack of inclusion of parasitic nonlinear processes (of which there are many) into the model. However, in this case, one should expect a better agreement at low intensities, which is not observed. By contrast, the beam-size study in Fig. 8 clearly shows improved agreement with larger beam size, suggesting that small beam size-effects are likely a strong contributor to the discrepancy between simulation and experiment. These effects, which are connected to transverse beam dynamics such as diffraction and self-focusing were not included in the present model for the sake of computing speed, highlighting the need of higher dimensionality in the model. In addition, as can be seen in Figs. 4–6, the pulse trains in the *regen configuration* performed significantly worse than in the *4-pass configuration* for all cases. Specifically, the data from the *4-pass configuration* is about 20–40% lower than prediction, while the data from the *regen configuration* is lower by a factor of about 2–3. Major differences between the pulse-trains in the two configurations which could explain the performance difference were not noticed during the experiments. However later analysis pointed to different amounts of nonlinear phase accrued in the amplifiers as a likely culprit. Due to the lower energy achievable in the *regen configuration*, the system was pushed to smaller beam sizes and higher peak intensities in order to have sufficient intensity for the experiments.

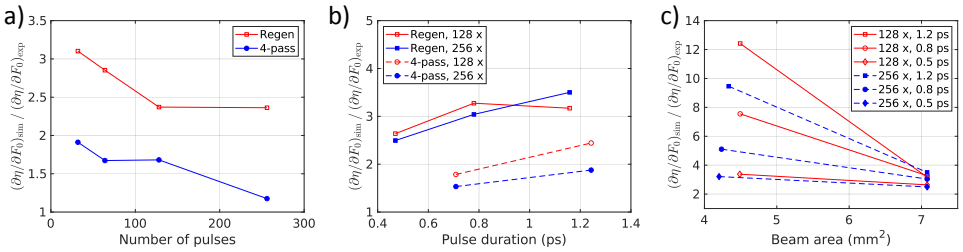


**Fig. 8.** Ratio of simulated to experimental performance as a function of (a) number of pulses, (b) pulse duration and (c) optical beam size. Results from both regen and 4-pass configurations are plotted. The graphs show that the agreement between simulation and experiment worsens as the number of pulses reduces, as the pulse duration increases and as the beam size reduces, for all configurations.

Finally, the unexplored parameter space is quite large and a number of key parameters remain to be studied in detail. Among these are the length, temperature and material of the conversion medium. In addition, a systematic study of the CE saturation behavior and the damage threshold under different conditions is highly important for determining the boundaries of the accessible parameter space. The analysis presented here was framed in terms of both fluence-based and intensity-based performance metrics because of the presence of multiple damage mechanisms, some of which limit the fluence (e.g., the photorefractive effect [26]) and some of which limit the intensity (e.g., self-focusing, self-phase modulation, parasitic nonlinear optical conversion, etc.). It should be noted that the analysis here was restricted to a range of fluences and intensities for which the CE displays a linear dependence (where the undepleted pump approximation is applicable) in order to allow effective comparison with theory. At higher fluence and intensity, however, the CE saturates (i.e., the performance metrics $\partial\eta_{THz}/\partial F_0$ and $\partial\eta_{THz}/\partial I_0$ reduce to zero or become negative). The parameter dependence of the saturation is also not fully explored but is highly relevant to a complete understanding of the conversion process. Ultimately, to reach a global optimization of the conversion efficiency requires knowledge of the parameter dependences in both the linear and saturation regimes as well as the parameter limits associated with damage.

This work targets the first of these requirements, precisely mapping out the dependence of conversion efficiency on pulse-train frequency, number of pulses and pulse duration. This

Optics EXPRESS

study was enabled by development of a pulse-train-based optical driver with a high degree of flexibility for tuning parameters. As a result of the optimization a maximum performance of $\partial\eta_{THz}/\partial F_0 \approx 2.5 \times 10^{-3}$ %/(mJ/cm$^2$) was achieved which is comparable to the performance achieved of $\partial\eta_{THz}/\partial F_0 \approx 2.1 \times 10^{-3}$ %/(mJ/cm$^2$) using the two line system which produced a record efficiency of 0.89% at a fluence of over 450 mJ/cm$^2$. The pulse-train optimum corresponds to a respectable efficiency of just over 0.31% at a fluence of 150 mJ/cm$^2$, which is compatible with long term operation. Further development of the pulse-train system is currently under way, which will lead to greater flexibility in pulse train number as well as higher pulse energy and greater amplitude regularity which are expected to push performance significantly higher.

**Funding.** European Research Council (609920, ERC Synergy Grant "AXSIS", FP7/2007-2013); Deutsche Forschungsgemeinschaft (Project No. 405983224).

**Disclosures.** The authors declare no conflicts of interest.

**Data availability.** Data underlying the results presented in this paper are not publicly available at this time but may be obtained from the authors upon reasonable request.

## References

1. T. Kampfrath, K. Tanaka, and K. A. Nelson, "Resonant and nonresonant control over matter and light by intense terahertz transients," Nat. Photonics **7**(9), 680–690 (2013).
2. E. A. Nanni, W. R. Huang, K. H. Hong, K. Ravi, A. Fallahi, G. Moriena, R. J. Dwayne Miller, and F. X. Kärtner, "Terahertz-driven linear electron acceleration," Nat. Commun. **6**(1), 8486 (2015).
3. X. Wu, D. Kong, S. Hao, *et al.*, "Generation of 13.9-mJ Terahertz Radiation from Lithium Niobate Materials," Adv. Mater. **35**(23), 2208947 (2023).
4. B. Zhang, Z. Ma, J. Ma, X. Wu, C. Ouyang, D. Kong, T. Hong, X. Wang, P. Yang, L. Chen, Y. Li, and J. Zhang, "1.4-mJ High Energy Terahertz Radiation from Lithium Niobates," Laser Photonics Rev. **15**(3), 2000295 (2021).
5. C. Vicario, B. Monoszlai, and C. P. Hauri, "GV/ m single-cycle terahertz fields from a laser-driven large-size partitioned organic crystal," Phys. Rev. Lett. **112**(21), 213901 (2014).
6. M. Shalaby and C. P. Hauri, "Demonstration of a low-frequency three-dimensional terahertz bullet with extreme brightness," Nat. Commun. **6**(1), 5976 (2015).
7. M. C. Hoffmann and J. A. Fülöp, "Intense ultrashort terahertz pulses: Generation and applications," J. Phys. D: Appl. Phys. **44**(8), 083001 (2011).
8. S. Carbajo, J. Schulte, X. Wu, K. Ravi, D. N. Schimpf, and F. X. Kärtner, "Efficient narrowband terahertz generation in cryogenically cooled periodically poled lithium niobate," Opt. Lett. **40**(24), 5762–5765 (2015).
9. S. W. Jolly, N. H. Matlis, F. Ahr, V. Leroux, T. Eichner, A. L. Calendron, H. Ishizuki, T. Taira, F. X. Kärtner, and A. R. Maier, "Spectral phase control of interfering chirped pulses for high-energy narrowband terahertz generation," Nat. Commun. **10**(1), 2591 (2019).
10. F. Ahr, S. W. Jolly, N. H. Matlis, S. Carbajo, T. Kroh, K. Ravi, D. N. Schimpf, J. Schulte, H. Ishizuki, T. Taira, A. R. Maier, and F. X. Kärtner, "Narrowband terahertz generation with chirped-and-delayed laser pulses in periodically poled lithium niobate," Opt. Lett. **42**(11), 2118–2121 (2017).
11. F. Lemery, T. Vinatier, F. Mayet, R. Aßmann, E. Baynard, J. Demailly, U. Dorda, B. Lucas, A. K. Pandey, and M. Pittman, "Highly scalable multicycle THz production with a homemade periodically poled macrocrystal," Commun. Phys. **3**(1), 150 (2020).
12. K. L. Vodopyanov, M. M. Fejer, X. Yu, J. S. Harris, Y. S. Lee, W. C. Hurlbut, V. G. Kozlov, D. Bliss, and C. Lynch, "Terahertz-wave generation in quasi-phase-matched GaAs," Appl. Phys. Lett. **89**(14), 141119 (2006).
13. J. R. Danielson, A. D. Jameson, J. L. Tomaino, H. Hui, J. D. Wetzel, Y. S. Lee, and K. L. Vodopyanov, "Intense narrow band terahertz generation via type-II difference-frequency generation in ZnTe using chirped optical pulses," J. Appl. Phys. **104**(3), 33111 (2008).
14. W. Tian, G. Cirmi, H. T. Olgun, *et al.*, "μJ-level multi-cycle terahertz generation in a periodically poled Rb:KTP crystal," Opt. Lett. **46**(4), 741 (2021).
15. C. D. W. Mosley, D. S. Lake, D. M. Graham, S. P. Jamison, R. B. Appleby, G. Burt, and M. T. Hibberd, "Large-area periodically-poled lithium niobate wafer stacks optimized for high-energy narrowband terahertz generation," Opt. Express **31**(3), 4041 (2023).
16. M. Seo, J. H. Mun, J. Heo, and D. E. Kim, "High-efficiency near-infrared optical parametric amplifier for intense, narrowband THz pulses tunable in the 4 to 19 THz region," Sci. Rep. **12**(1), 16273–7 (2022).
17. N. E. Yu, K. S. Lee, D. K. Ko, C. Kang, S. Takekawa, and K. Kitamura, "Temperature dependent narrow-band terahertz pulse generation in periodically poled crystals via difference frequency generation," Opt. Commun. **284**(5), 1395–1400 (2011).
18. K. Ravi, M. Hemmer, G. Cirmi, F. Reichert, D. N. Schimpf, O. D. Mücke, and F. X. Kärtner, "Cascaded parametric amplification for highly efficient terahertz generation," Opt. Lett. **41**(16), 3806 (2016).
19. K. Ravi, D. N. Schimpf, and F. X. Kärtner, "Pulse sequences for efficient multi-cycle terahertz generation in periodically poled lithium niobate," Opt. Express **24**(22), 25582–25607 (2016).

Optics EXPRESS

20. K. Ravi and F. X. Kärtner, "Terahertz-induced cascaded interactions between spectra offset by large frequencies," Opt. Express **27**(14), 19254 (2019).
21. K. Ravi and F. X. Kärtner, "Raman Shifting Induced by Cascaded Quadratic Nonlinearities for Terahertz Generation," Laser Photon. Rev. **14**(11), 2000109 (2020).
22. S. W. Jolly, F. Ahr, K. Ravi, N. H. Matlis, F. X. Kärtner, and A. R. Maier, "On the effect of third-order dispersion on phase-matched terahertz generation via interfering chirped pulses," Opt. Express **27**(24), 34769 (2019).
23. H. T. Olgun, W. Tian, G. Cirmi, K. Ravi, C. Rentschler, H. Çankaya, M. Pergament, M. Hemmer, Y. Hua, D. N. Schimpf, N. H. Matlis, and F. X. Kärtner, "Highly efficient generation of narrowband terahertz radiation driven by a two-spectral-line laser in PPLN," Opt. Lett. **47**(10), 2374 (2022).
24. K. L. Vodopyanov, "Optical generation of narrow-band terahertz packets in periodically-inverted electro-optic crystals: conversion efficiency and optimal laser pulse format," Opt. Express **14**(6), 2263 (2006).
25. M. Unferdorben, Z. Szaller, I. Hajdara, J. Hebling, and L. Pálfalvi, "Measurement of Refractive Index and Absorption Coefficient of Congruent and Stoichiometric Lithium Niobate in the Terahertz Range," J. Infrared, Millimeter, Terahertz Waves **36**(12), 1203–1209 (2015).
26. Y. Furukawa, K. Kitamura, A. Alexandrovski, R. K. Route, M. M. Fejer, and G. Foulon, "Green-induced infrared absorption in MgO doped LiNbO3," Appl. Phys. Lett. **78**(14), 1970–1972 (2001).